Robust hybrid bismuth perovskites as potential photocatalysts for overall water splitting

Antonio J. Chacón-García[1], Herme G. Baldovi[2], Artem A. Babaryk[1], Antonio Rodríguez-Diéguez[3], Sergio Navalón[2], Yolanda Pérez[*,1,4], Hermenegildo García[*,5], Patricia Horcajada[*,1]

[1]*Advanced Porous Materials Unit, IMDEA Energy Institute, Avda. Ramón y Cajal 3, 28935 Móstoles, Madrid, Spain*

[2]*Departamento de Química, Universitat Politècnica de València, 46022 València, Spain*

[3]*Departamento Química Inorgánica, Universidad de Granada, 1807, Granada, Spain*

[4]*Departamento de Biología y Geología, Física y Química Inorgánica. ESCET. Universidad Rey Juan Carlos, 28933 Móstoles, Madrid, Spain*

[5]*Instituto de tecnología química CSIC-UPV, Universitat Politècnica de València (UPV), 46022, Spain.*

patricia.horcajada@imdea.org; hgarcia@qim.upv.es; yolanda.cortes@urjc.es

Abstract

Organic-inorganic hybrid perovskites have gained great attention as promising photocatalysts for hydrogen generation. However, due to their poor stability in water, the use of aqueous hydrohalic acid solutions is specifically required for an efficient hydrogen evolution. Herein, three novel photoactive lead-free hybrid perovskites based on bismuth and triazolium cations (denoted as IEF-15, IEF-16, and IEF-17) were synthesized and fully characterized (structural, compositional, optical, etc.). Further, these solids were proposed as photocatalysts for the challenging gas phase overall water splitting reaction (OWS). Accordingly, IEF-16 thin films exhibited a remarkable photocatalytic activity in both H_2 and O_2 evolution, as a consequence of its appropriate bandgap and energy-band alignment, achieving hydrogen evolution rates of 846 and 360 µmol $H_2 \cdot g^{-1}$ after 24 h under UV-vis irradiation or simulated solar irradiation, respectively. This study additionally highlights the remarkable structural and photochemical stability of IEF-16 under different operational conditions (*i.e.* water volume, irradiation and temperature), paving the way for green hydrogen production from OWS using perovskite-based photocatalysts.

Keywords: Bismuth-based hybrid perovskites, thin films, photocatalysis, overall water splitting, green hydrogen.

1. Introduction

The search for alternative energy resources to the conventional fossil fuels has become a relevant challenge in the last decade. The main reasons reside in the scarcity of fossil fuels, recent extreme weather and global energy crisis, with the urgent need to reduce greenhouse emissions in order to achieve carbon neutrality by 2050 [1]. As an emerging alternative, hydrogen is considered as a clean and efficient energy vector, since it provides a high energy content (122 $KJ \cdot g^{-1}$), which is 2.75 times superior to that obtained with conventional fuels [2]. Nonetheless, the current industrial hydrogen production routes are still controversial: from the ~60 million tons of H_2 annually produced, 96% is generated from fossil fuels (*e.g.* steam methane reforming, pyrolytic processes of natural gas, liquid hydrocarbons or coal) [3]. Recently, the hydrogen production from water using renewable sources (*i.e.* solar power) has gained a rising significance, developing cost-effective routes and reducing CO_2 emissions [4]. Thus, solar-driven hydrogen production technologies[5], such as photocatalysis, photoelectrocatalysis, photovoltaic-electrocatalysis, solar thermocatalysis, or photothermal catalysis, are considered effective approaches to produce green hydrogen.

In particular, photocatalytic overall water splitting (OWS) is a promising and growing technology which is desirable due to its low cost and simplified process in comparison with other technologies, such as electrocatalysis or thermocatalysis [6]. The photocatalytic mechanism starts when the solar light irradiation generates excited electrons in the conduction band of a semiconductor, followed by the separation of electrons and holes with the non-stop migration through the surface of the material. Then, the photoexcited electrons react with the protons to produce hydrogen (HER) and, parallelly, the holes oxidize water to generate oxygen (OER) [7].

In this sense, organic-inorganic hybrid halide perovskites represent a wide family of semiconductors derived from the general formula ABX_3 (A = organic cation, B = metal cation, and X = halide anion). Specially, lead-based perovskites have been widely explored for the development of solar cells owing to their outstanding optoelectronic properties, tunable bandgap, high absorption coefficient and exceptional carrier mobility [8], reaching 25.8% of power conversion efficiency (PCE) [9]. In recent years, their scope of application has been extended to other fields such as photonics [10], optoelectronic devices (*e.g.* LEDs) [11], sensing [12] and photocatalysis [13], among others. Nevertheless, the main limitations of lead-based perovskites reside in their low stability under atmospheric and humid conditions and the associated lead-toxicity, severely impacting on the environment and human health [14]. Thereby, a potential suitable alternative could be the Pb^{2+} replacement by a greener metal, such as the Bi^{3+}, with similar electronic configuration, electronegativity and ionic radius [15].

Bismuth halide perovskites englobe a wide variety of general formulas (including $ABiI_4$, $ABiI_5$, ABi_2I_9, ABi_2I_7, $A_3Bi_2I_9$, $A_4Bi_4I_{16}$), and different dimensionalities from isolated octahedra in 0D to 2D layered structures and 3D networks [16–18].

Despite the excellent visible-light absorption of these Bi-based perovskites, their use as photocatalysts for OWS is strongly limited by their intrinsic aqueous instability. To prevent degradation, most of the efforts have been focused on: i) using sacrificial agents as aqueous hydrohalic acid (HBr or HI) solutions and ii) adding H_3PO_2 to reduce Br_3^- or I_3^- ions generated during the reaction. For example, DMA_3BiI_6 (DMA = $(CH_3)_2NH_2$) [19] and $MA_3BiI_2I_9$ (MA = CH_3NH_3) [20] materials have been investigated for HER by HI splitting photocatalytic reaction, exhibiting a catalytic activity of 15 and 12.2 $\mu mol \cdot g^{-1} \cdot h^{-1}$, respectively. Using Pt as cocatalyst in the case of $MA_3BiI_2I_9$, H_2 photogeneration was enhanced up to 169.2 $\mu mol\ g^{-1} \cdot h^{-1}$. More recently, Zhao *et al*. [21] have proven that DA_3BiI_6 (DA = $(CH_3)_2NH_2$) is able to oxidize I^- ions from DAI solution, reaching a H_2 evolution rate of 5.7 $\mu mol \cdot h^{-1}$ in the presence of HI in DAI solution and $PtCl_4$ co-catalyst. Moreover, other systems based on perovskite materials have showed an enhanced photocatalytic H_2 evolution activity such as Cs-Cu-Cl perovskite quantum dots [22], $MoSe_2$/$MAPbBr_{3-x}I_x$ [23] and Pt/$FAPbBr_{3-x}I_x$ [24]. Despite being HER high-efficient systems, the use of corrosive chemical agents brings major drawbacks, hindering their commercial application. In this regard, García et al. [25] have succeeded in obtaining 6 $\mu mol\ H_2 \cdot g^{-1}$ applying a copper-based perovskite ($MA_2CuCl_2Br_2$) photocatalyst, in the absence of any sacrificial agent and co-catalyst, which is the only reported example on hybrid halide perovskites applied for OWS photocatalysis. Even further, to the best of our knowledge, there are no bismuth-based hybrid halide perovskites proposed yet for OWS.

With this in mind, we present for the first-time novel organic-inorganic hybrid bismuth perovskites as photocatalysts for gas phase OWS. Thus, three original perovskites based on different Bi(III) inorganic frameworks (*i.e.* $[BiI]_5$ or $[BiI_4]$) and azolium cations (*i.e.* triazolium-TrzH and dimethylpyrazolium-DmpzH) were synthesized and denoted as $(TrzH)_2[BiI]_5$ or IEF-15, $TrzH[BiI_4]$ or IEF-16, and $DmpzH[BiI]_4$ or IEF-17 (IEF stands for IMDEA Energy Frameworks). Structural and spectroscopic characterizations of the prepared perovskites were performed in order to provide new insights and a better understanding of their photocatalytic properties.

The synthesized perovskites showed an optimal bandgap to perform solar-driven reactions, highlighting the IEF-16 solid as the most active photocatalyst for HER (2.86 $\mu mol\ g^{-1} \cdot h^{-1}$). This material, deposited forming 450 nm-thickness thin films, was able to produce 34.5 µmol of $H_2 \cdot g^{-1} \cdot h^{-1}$. This, together with its robustness under humid environments (70% relative humidity-RH) and long-term ambient conditions (> 1 year), makes IEF-16 an efficient and non-toxic OWS photocatalyst for O_2 and H_2 evolution reactions.

2. Experimental section

2.1. Materials

All reagents and solvents were purchased from commercial sources and used without further purification: bismuth(III) oxide 99.9% (Acros Organics), bismuth(III) nitrate pentahydrate 98% (Acros Organics), hydroiodic acid 57% w/w (Acros Organics), 1H-1,2,4-triazole-3,5-diamine >98% (Sigma Aldrich), 3,5-dimethylpyrazole 99% (Alfa Aesar), absolute ethanol (VWR), N-N'-dimethylformamide (Acros Organics) and diethyl ether (Fisher Scientific).

2.2. Synthesis of IEF-15

Bi_2O_3 (0.47 g, 1 mmol) was added to a round-bottom flask with 10 mL of absolute ethanol. The dispersion was stirred for 10 min and then, HI (57% wt. solution, 1.3 mL, 9.8 mmol) was added. The resulting solution was stirred for 30 min and then, 3,5-diamino-1,2,4-triazole (0.20 g, 4 mmol) was added to the solution. The mixture was stirred for 10 min and then, heated at 80 ºC for 30 min. Single crystals of $(TrzH)_2[BiI]_5$ (denoted as IEF-15) were growth by the evaporation of ethanol at room temperature and washed with diethyl ether. Yield: 82.0%. $(C_2H_6N_5)_2BiI_5$ calc. (%): C, 4.52; N, 13.22; H, 1.18; found (%): C, 4.60; N, 13.42; H: 1.16.

2.3. Synthesis of IEF-16

The synthesis of $TrzH[BiI_4]\cdot H_2O$ (named as IEF-16) was carried out following the same synthetic protocol to that described for IEF-15 but using a molar ratio 1:2 of Bi_2O_3 and 3,5-diamino-1,2,4-triazole. Single crystals were obtained by slow evaporation of the solution at room temperature. Yield: 51.0%. $(C_2H_6N_5)BiI_4\cdot H_2O$ calc. (%): C, 2.88; N, 8.39; H, 0.97; found (%): C, 2.88; N, 8.64; H: 0.96.

A new phase of IEF-16, denoted dehydrated IEF-16 phase, was obtained when IEF-16 was heated at 100 °C for 90 min under vacuum. The color of the material changed from red to reddish black, as consequence of the formation of the dehydrated phase ($TrzH[BiI_4]$).

2.4. Synthesis of IEF-17

$Bi(NO_3)_3\cdot 5H_2O$ (0.68 g, 1.4 mmol) was dispersed in 10 mL of absolute ethanol and HI (57% wt. solution, 1.2 mL, 8.4 mmol) was added under stirring at room temperature. The resulting solution was stirred for 30 min and then, 3,5-dimethylpyrazole (0.13 g, 1.4 mmol) was added. The suspension was heated at 80°C for 30 min, getting a clear solution. Red crystals of $DmpzH[BiI]_4$ (denoted IEF-17) were obtained by the cooling of the solution, washed with diethyl ether

and dried under nitrogen flow at room temperature. Yield: 72.8%. $(C_5H_9N_2)BiI_4$ calc. (%): C, 7.38; N, 3.44; H, 1.11; found (%): C, 7.48; N, 3.13; H: 1.12.

2.5. Preparation of thin films

IEF-16 was dissolved in *N-N'*-dimethylformamide (DMF; 1 M) and then, 40 µL of this perovskite solution was deposited in a pre-cleaned glass substrate (1.5 x 1.5 cm) by using a simple and fast spin-coating method (3000 rpm for 30 s) under ambient conditions. Finally, the deposited material was annealed at 110ºC for 15 min to form a homogenous film.

2.6. General Instrumentation

Powder X-ray diffraction (PXRD) patterns were collected from 5 to 55° (2Θ) using an Empyrean (PANALYTICAL) diffractometer, equipped with a PIXce3D detector with a radiation source of CuK_α (Ni_β-filter, λ = 1.5406 Å) and operating at 45 kV and 40 mA. Temperature-dependent X-ray diffraction (TDXRD) patterns were recorded using D8 Advance (Bruker AXS) θ-2θ diffractometer with CuK_α radiation source (λ = 1.5406 Å) and equipped with an LYNXEYE XE detector. Samples were placed in a circular alumina boat, with a heating rate of 5° min^{-1} from 30 to 270 °C inside an Anton Paar XRK 900 chamber under Ar at 50 $mL \cdot min^{-1}$. The diffraction angles aperture was 5-55°. Thermogravimetric analyses (TGA) were carried out using a Q600 analyzer (TA Instruments) with a heating rate of 5 $°C \cdot min^{-1}$ under Ar from 25 to 400 ºC. Fourier transform infrared (FTIR) spectra were collected in a Thermo Scientific Nicolet 6700 spectrophotometer in attenuated total reflectance (ATR) mode from 1000 to 4000 cm^{-1} with 64 accumulations *per* scan. RAMAN spectra from 0 to 200 cm^{-1} were collected in a JASCO NRS-5100 spectrophotometer working at x100 magnification. Diffuse reflectance ultraviolet-visible (DRUV-VIS) spectra were recorded on a Varian Cary 5000 spectrophotometer (Agilent Technologies, Santa Clara, CA, USA) with an integrating sphere and using $BaSO_4$ as a reference. Bandgap values (E_g) were calculated by applying the Kubelka-Munk equation. Photoluminescence spectra were acquired using a Perkin-Elmer LS 55 fluorescence spectrometer with a Xe lamp at 405 nm excitation wavelength (cut wavelength 430 nm). Photocurrent response measurements were carried out using a Hamamatsu lamp equipped with a 150 W Xe/Hg bulb and an AM 1.5 G filter and using a 5 mM solution of $NaBF_4$ in dichloromethane as an electrolyte. Scanning electron microscopy (SEM) images were collected on a Hitachi TM-100 microscope and High-Resolution Transmission Electron Microscopy (HRTEM) were obtained on a JEOL JEM2100F instrument. Atomic force microscopy (AFM) measures were acquired using a Park XE-100 atomic force microscope with NTMDT NSG30 non-contact tip with a force constant of 40 $N \cdot m^{-1}$, a resonant frequency of 320 kHz and a tip radius less than 10 nm.

2.7. Single-crystal X-ray diffraction (SCXRD)

Red crystals for IEF-15, IEF-16 and IEF17 were mounted on a glass fiber and used for data collection on a Bruker D8 Venture with a photon detector equipped with graphite monochromated MoK_α radiation (λ=0.71073 Å). The data reduction were performed with the APEX2 software [26] and corrected for absorption using SADABS [27]. Crystal structures were solved by direct methods using the SIR97 program [28] and refined by full-matrix least-squares on F^2 including all reflections using anisotropic displacement parameters by means of the WINGX crystallographic package [29,30] The OLEX2 software [31] was used for the final refinement. Generally, anisotropic temperature factors were assigned to all atoms except for hydrogen atoms, which are riding their parent atoms with an isotropic temperature factor arbitrarily chosen as 1.2 times that of the respective parent. Final R(F), wR(F2) and goodness of fit agreement factors, details on the data collection and analysis can be found in Table S1. Crystallographic data (excluding structure factors) for the structures reported in this paper have been deposited with the Cambridge Crystallographic Data Centre as supplementary publication n. CCDC 1891467, 1891468 and 1891469. Copies of the data can be obtained free of charge on application to the Director, CCDC, 12 Union Road, Cambridge, CB2 1EZ, U.K. (Fax: +44-1223-335033; e-mail: deposit@ccdc.cam.ac.uk).

2.8. Ultraviolet photoelectron spectroscopy (UPS)

UPS measurements were carried out in a SPECS GmbH photoelectron spectrometer equipped with an ultra-high vacuum (UHV) system and an energy analyzer PHOIBOS 150 9MCD. He I (21.2 eV) was employed as photon source with an energy pass of 2 eV. The UPS instrument was calibrated by referencing the Fermi level of Ag at 0 eV.

2.9. X-ray photoelectron spectra (XPS)

XPS measurements were performed using a SPECS spectrometer equipped with an MCD-9 detector and a monochromatic Al (Kα= 1486.6 eV) X-ray source. Spectra deconvolution was performed with the CASA software and using the C 1s peak at 284.4 eV as binding energy reference [32].

2.10. Gas phase photocatalytic water splitting

Photocatalytic overall water splitting experiments were carried out in a glass reactor (30 mL) and employing a gas water phase. The photocatalyst (50 mg for the powder or 0.5 mg for the thin film) was carefully placed in the center of the reactor, suspended above liquid water. Then, the reactor was purged with argon gas prior to the reaction and pressurized to 1 bar. The photocatalysts were irradiated by a Hamamatsu light system equipped with a Hg-Xe 150 W valve and optic fiber (Hamamatsu spotlight source L9566-04 and light guide A10014-50-0110). In the experiments with simulated sunlight irradiation, an AM 1.5G light

filter (Lasing ref. 81094) was placed between the optic fiber and the photoreactor. After the desired reaction time, gas samples were analyzed using an Agilent 490 MicroGC equipped with two channels and thermal conductivity detectors. The first channel, equipped with a MolSieve 5A˚ column, allowed the quantification of H_2, O_2, N_2, and CO, while the other channel, equipped with a Pore Plot Q column, allowed the determination of CO_2, CH_4, and short-chain hydrocarbons. Quantification was performed using calibration plots.

3. Results and discussion

3.1. Synthesis, structural and morphological characterization

It is well-known that the organic cation of hybrid organic-inorganic perovskites plays a relevant role shaping the orientation of the inorganic chains and, consequently, the dimensionality and the optical properties of the final material [33]. In this regard, three novel semiconducting perovskite materials were synthesized by a simple and fast procedure (ethanol, 80ºC, 30 min; see experimental section for further details) from either Bi_2O_3 and 3,5-diamino-1,2,4-triazole (Trz; molar ratio bismuth precursor : organic compound = 1:4 and 1:2 for IEF-15 and IEF-16, respectively) or from $Bi(NO_3)_3{\cdot}5H_2O$ and 3,5-dimethylpyrazole (Dmpz) with stoichiometric molar ratio (IEF-17). Single crystals were isolated and their crystalline structure unveiled by single crystal X-ray diffraction (SCXRD), confirming the purity of the phases by powder X-ray diffraction (PXRD; Fig. S1).

SCXRD analysis revealed that all structures are built of one-dimensional (1D) chains of edge- or corner-sharing BiI_6 octahedra chains. IEF-15 ($(TrzH)_2[BiI]_5$) crystallizes in a triclinic system whose unit cell parameters are a = 8.8581(5), b= 10.9751(6), c = 11.6999(7) (Table S1). Bismuth atoms are coordinated with six iodine atoms in an octahedral disposition building up polymeric ribbon anions $[BiI_{5/6}]_\infty$. The structure of corner-sharing octahedra adopts a one-dimensional (1D) zig-zag ribbon orientation (Fig. 1), where two bismuth atoms from adjacent octahedrons are separated from each other by 6.4756(8) Å. The $[BiI_5]^{2-}$ moieties are charge-balanced along the *a*-axis by two triazolium cations. Thus, the position adopted by the cations, facing each other over and down between the inorganic chains, plays a comprising effect over octahedral units by the formation of short N-H···I interactions (in the range of 2.7922(9)-2.9951(11) Å) with the non-shared corners of the octahedra. Bi-I distances are enclosed between 2.9444(9) and 3.2384(4) Å, the shortest distances correspond to bismuth and terminal iodine atoms and the longest ones to bismuth and bridging iodine atoms. Additionally, iodine atoms in *cis* orientation form I-Bi-I angles from 84.074(18) to 96.23(3)°, while in trans configuration the angles vary from 173.12(2) to 178.65(3)° (Table S2). These parameters indicate a significant distortion in the BiI_6 octahedra, which has already been observed in other iodobismuthate derivatives containing $[BiI_5]^{2-}$ chains (see Table S3). It is important to note that in the structure of IEF-15, the Bi-I-Bi angles formed by two bismuth atoms from adjacent octahedra are

180(0)º, which is rarely found in structures based on iodobismuthates (Table S3) [34].

On the other hand, SCXRD analysis of IEF-16 (TrzH[BiI_4]·H_2O) points out that this perovskite material also crystallizes in the triclinic system with unit cell parameters a = 7.4157(6), b = 9.9375(7), and c = 10.4862(7) (Table S1). However, in this case, the structure contains one-dimensional (1D) ribbon anions $[BiI_{4/6}]_\infty$ with BiI_6 octahedra sharing edges, where two iodine atoms (one axial and one equatorial) are linked with an adjacent BiI_6 octahedra (Fig. 2). The Bi-I distances range is wider than that observed in the IEF-15, with Bi-I bond lengths ranging from 2.9182(11) to 3.3019(10) Å, being more marked in Bi-I (bridging) distances. The *cis* I-Bi-I angles are comprised between 83.61(4)-95.48(3)°, while in *trans* position they oscillate between 172.81(3)-176.61(3)° (Table S2). Accordingly, the structure displays distorted octahedra, possibly due to the repulsion of bismuth atoms from the adjacent BiI_6 octahedron [35] and, the position adopted by the triazolium cations. The structure of $(AmV)_3(BiI_6)_2$ (AmV = 4,4′-amino-bipyridinium) [36], which serves as a fitting example of an undistorted octahedral geometry, comprises Bi-I distances ranging between 3.06−3.09 Å and I−Bi−I bond angles close to 90°. In addition, the organic cations form interconnected parallel chains by the formation of hydrogen bonds with water molecules (N-H···O-H interactions of 1.949(11) Å). HRTEM images of IEF-16 was performed as a representative sample (Fig. S2), showing a d-spacing of 0.227 nm. Besides, the SAED pattern evidences the crystalline nature of the bismuth-based perovskite.

Similarly to the IEF-16 structure, IEF-17 (DmpzH[BiI]$_4$) is also composed of $[BiI_4]^-$ chains of edge-sharing BiI_6 units (Fig. 3), but IEF-17 belongs to the monoclinic system with unit cell parameters a = 14.4660(7), b = 13.4478(7), and c = 7.8692(3) (Table S1). Again, bond angles and distances in IEF-17 show a substantial deviation from an octahedral geometry. In this case, the Bi-I distances range is slightly shorter than that found in the structure of IEF-16, ranging from 2.9040(6) to 3.3281(6) Å, while the Bi-I-Bi bond angle increases to 96.758(14)º, rising the octahedra distortion (Table S2). Pyrazolium cations in IEF-17 adopt a different position compared to triazolium ones, which are linked to each other by a water molecule. In contrast, pyrazolium cations form short interactions between the protonated amino group and the bridging iodine of the BiI_6 octahedra in both, axial and equatorial positions, by a N-H···I distance of 2.7448(5) and forming angles of 165.9(6)º.

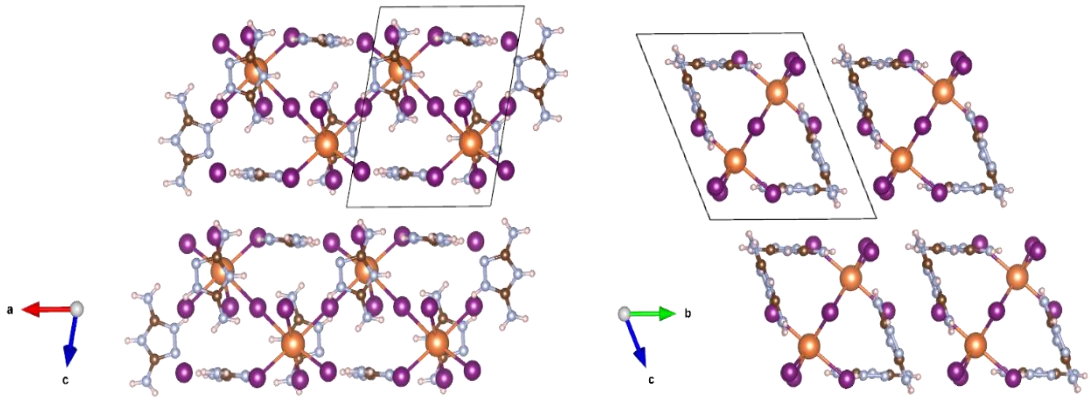

Fig. 1 Structure of IEF-15 (Bi, I, N, C and H atoms are represented by orange, purple, blue, brown and pink ellipsoids, respectively).

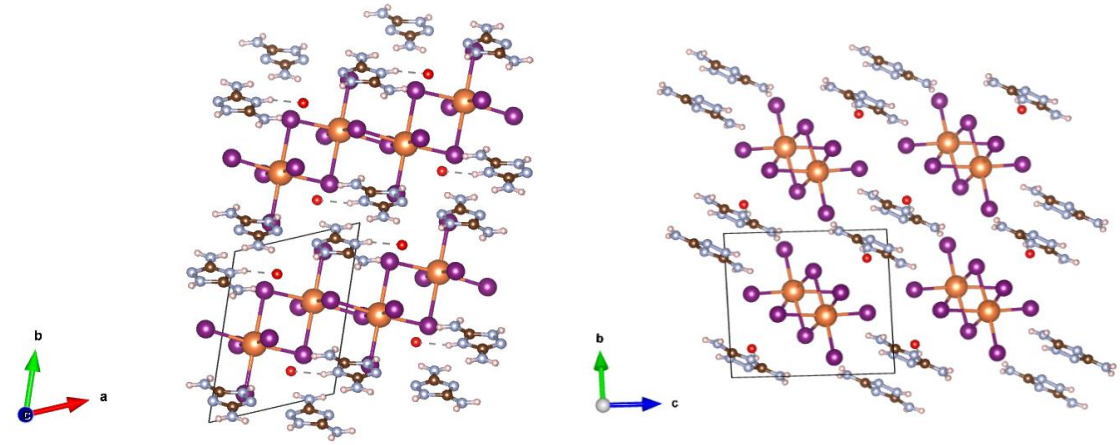

Fig. 2 Structure of IEF-16 (Bi, I, N, C and H atoms are represented by orange, purple, blue, brown and pink ellipsoids, respectively).

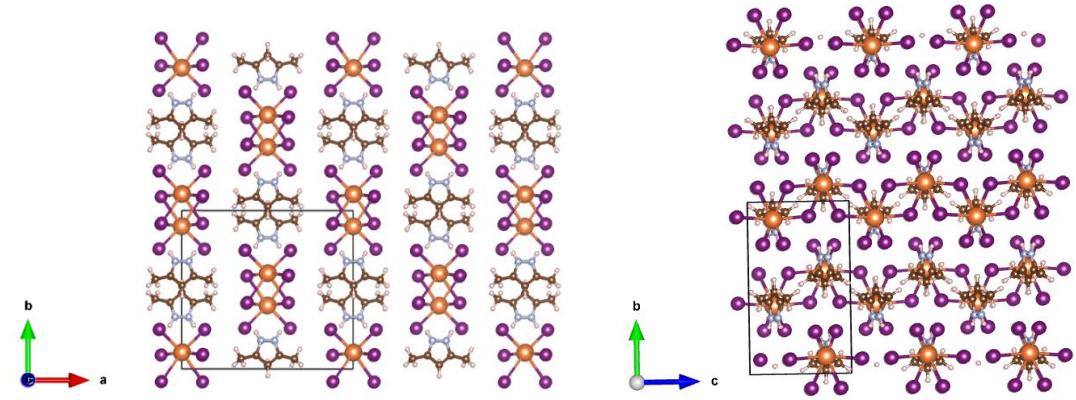

Fig. 3 Structure of IEF-17 (Bi, I, N, C and H atoms are represented by orange, purple, blue, brown and pink ellipsoids, respectively).

3.2. Spectroscopic characterization

The three perovskite materials were further characterized by different spectroscopic techniques (FT-IR, Raman, XPS, UV-Vis and photoluminescence). First, in the FT-IR spectra (Fig. S3), the N-H stretching vibrations are slightly shifted (3430–3300 cm^{-1} for IEF-15 and IEF-16, and 3300-3100 cm^{-1} for IEF-17) in comparison with those observed in the spectra of the free organic ligands. Besides, the spectrum of IEF-16 displays additional bands at 3560 and 1608 cm^{-1}, which are ascribed to the O-H stretching and deformation vibrations of the water molecules, respectively. Second, Raman spectra were collected to identify the vibrational modes of the iodobismuthate solids, appearing usually the scissoring (I-Bi-I and Bi-I-Bi) and stretching (Bi-I) modes below 200 cm^{-1} [37]. Hence, in the Raman spectra of the bismuth-based hybrid materials (Fig. S4), the Bi–I stretching mode of the terminal iodide atoms is observed as an intense band at 152, 151 and 154 cm^{-1} for IEF-15, IEF-16 and IEF-17, respectively.

Further, high resolution XPS characterization was performed (Fig. S5-S7), revealing the presence of the expected elements (Bi, C, N, and I), as well as oxygen atoms on the surface. Deconvolution of the Bi $4f_{5/2}$, Bi $4f_{7/2}$, I $3d_{3/2}$, and I $3d_{5/2}$ signals for the three materials showed a single peak, corresponding to Bi^{3+} and I^- oxidation states, respectively. There are no additional peaks at 157 eV (Bi $4f_{7/2}$) corresponding to the presence of metallic bismuth, revealing an outstanding chemical stability of the prepared bismuth-based perovskites under XPS conditions [38]. The C 1s signal of the three perovskites can be deconvoluted in two peaks at binding energies of 284.5 and 288 eV, attributed to C=N and C-N of the triazolium and pyrazolium cations, respectively. Similarly, in the deconvolution of the N 1s signal, two peaks are observed for IEF-15 and IEF-16, corresponding to the N-C (399.5 eV) and the N=N (401 eV) of the triazole ring. In agreement with the structure, the N 1s signal for IEF-17 appears as a single peak at around 401.5 eV, reflecting the pyrazole structure of the ligand. As previously mentioned, the O 1s band at 5.32 eV for the three bismuth-based perovskites could be attributed to adsorbed water on the surface.

In addition, the solids were characterized by UV-Vis spectroscopy in order to estimate their optical bandgap (E_g) [39] and energy bands (*i.e*. valence band maximum and conduction band minimum) [32]. These properties will determine the light-harvesting ability and the thermodynamic feasibility of semiconducting materials for the water oxidation and reduction, respectively. In perovskite materials, E_g strongly depends on the composition (halogen, metal or organic cation) [40] and the structure (dimensionality or lattice constant) [41]. Therefore, some factors, such as the electronegativity difference between Bi and I ions, the Bi-I-Bi angle or the Bi-I distance, can affect the E_g value [42] (Table S3) and then, their catalytic performances (see below). It is known that lead-based perovskites containing bulky cations (*i.e.* organic cations) are expected to expand the crystal lattice and decrease the E_g, while smaller cations (*i.e.* inorganic cations) are assumed to contract it, increasing the E_g [43]. In this regard, E_g values of the bismuth-based perovskite materials were estimated by Tauc plots using the absorption spectra (Fig. 4a) and considering them as direct semiconductors [39].

The estimated optical bandgap (Fig. S8) of IEF-15 was lower than that obtained for IEF-16, evidencing the influence of the inorganic chain on the E_g value (*i.e*. 1.77 eV with $[BiI_5]^-$ *vs.* 2.09 eV with $[BiI_4]^-$, respectively. Other perovskites based on $[BiI_5]^-$ with comparable geometric parameters (Bi-I-Bi angle ~ 163º and Bi–I distance ~ 2.9-3.2 Å) showed similar bandgap values (*e.g.* hexane-1,6-diammonium pentaiodobismuth ($HDABiI_5$) 1.89 eV [44]; N-methyl-1,3-diaminopropanium pentaiodobismuth ($H_2MDAPBiI_5$) 1.83 eV [45]) (see Table S3). However, no significant variation of E_g was detected by only replacing the organic cation (2.09 for the triazolium in IEF-16 *vs*. 2.13 eV for the dimethylpyrazolium in IEF-17), which may be due to the similar size of both cations (~6.3 Å).

Finally, to gain a better understanding of their optical properties, photoluminescence (PL) spectroscopic studies were performed at room temperature (Fig. 4b). As can be seen, IEF-15 emits in the red spectral region (emission band at 660 nm) upon excitation at 405 nm, while the PL bands observed for IEF-16 and IEF-17 are blue-shifted at around 600 nm. The assumption of direct bandgaps for the bismuth-based perovskites is in accordance with PL emission bands which are close to the optical absorption edge.

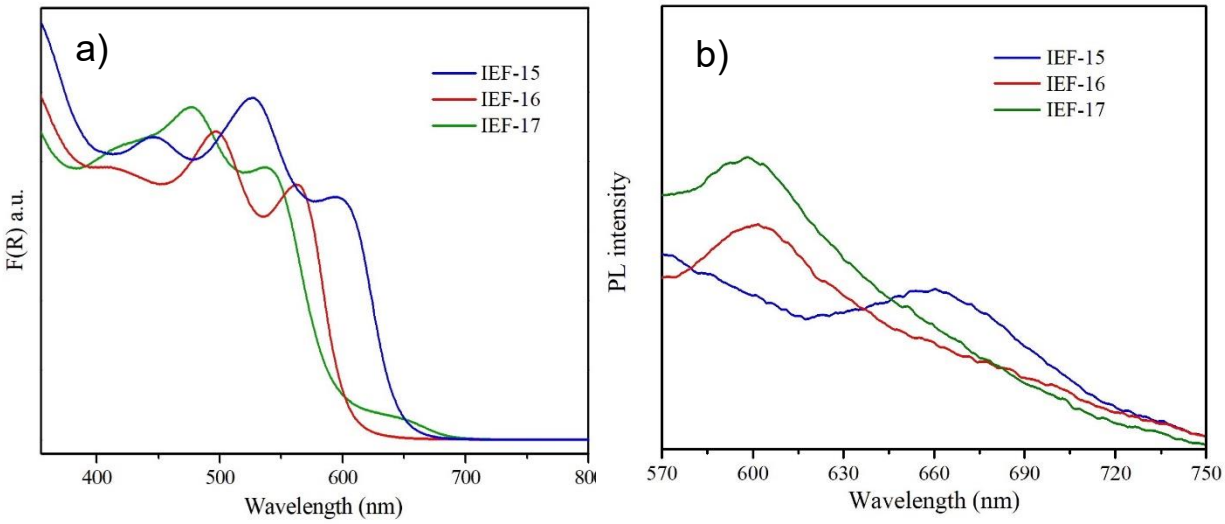

Fig. 4 a) UV-Vis diffuse spectra and b) photoluminescence plots for IEF-15, IEF 16 and IEF-17 samples

3.3. Stability studies

The thermal and chemical stability of perovskite materials are key parameters to consider in (photo)catalysis. It is known the often poor stability of lead iodide-based perovskite, leading to the formation of toxic species and limiting their application (*e.g.* decomposition of methylammonium lead iodide-based perovskite ($MAPbI_3$) at 85 ºC forming PbI_2) [46]. In contrast, bismuth-based hybrid perovskites exhibit a better thermal stability, keeping their structure at higher temperatures [47–49]. Hence, the thermal stability of the prepared perovskites

was investigated by means of thermogravimetric analysis (TGA; Fig. S9) and temperature-dependent x-ray diffraction (TDXRD; Fig S10). TGA reveals that IEF-16 has a greater thermal stability (until 250°C), whereas IEF-17 and IEF-15 start to decompose at 215 and 240 ºC, respectively. Besides, the TGA of IEF-16 shows a weight loss of 2.13% from 50 to 100ºC, which is associated with the departure of the water molecules of this structure ($TrzH[BiI_4]\cdot H_2O$; calc. 2.16%; (see inset Fig. S9). This fact is confirmed by TDXRD (Fig. S10b), where a phase transition is observed in the temperature range from 50 to 100°C, as a consequence of the IEF-16 dehydration, to finally obtain BiI_3 product at 220 ºC. The dehydrated IEF-16 phase might be the result of the triazolium reorganization into the structure, which instead of being connected by the formation of hydrogen bonds with adjacent water molecules, triazolium cations are found, in the newly adopted orientation, facing each other up and down and setting up by π interactions. A similar phase transformation upon water removal by heating has been previously observed by some of us in a different perovskite [39]. Additionally, IEF-15 and IEF-17 structures are maintained unaltered until 140 and 120 ºC, respectively.

On the other hand, lead-based perovskites are known also to exhibit a low stability under ambient environments, making necessary to prepare them under inert atmosphere. For example, when $MAPbI_3$ was exposed to ambient air, visual color changes were observed in only 5 days due to its degradation [50]. Thus, the stability of lead-based perovskites remains a challenge despite the large number of strategies proposed to improve it [51]. In contrast, bismuth-based perovskites show an enhanced stability in ambient air (*e.g.* $(C_6H_5NH_3)BiI_4$ is stable for 334 days [52], $(C_6H_5(CH_3)NH_2)_3Bi_2I_9$ for 300 days [53] and $Cs_2AgBiBr_6$ for 240 days [54]). In this sense, the prepared bismuth-based materials demonstrated an exceptional long-term stability, being stored under ambient conditions for 1 year (see XRD, Fig. S11), and demonstrating their superior stability in the presence of oxygen and humidity from the atmosphere.

3.4. Gas phase photocatalytic overall water splitting.

Considering the excellent chemical stability and the appropriate band gap of the synthesized perovskite materials, their photocatalytic activity was first screened for OWS using the bulk powder in deionized water (both in the liquid or gas phase) under simulated solar light irradiation at room temperature. As can be seen in Fig. 6a, the three materials show photocatalytic activity for both oxygen and hydrogen production in the absence of sacrificial agents, being IEF-16 the most efficient photocatalyst.

In an attempt to understand the best performance of IEF-16, the valence band maximum (VBM, E_υ^f) versus the Fermi level in each material was determined from UPS (see Fig. S12) [32]. The VBM position versus NHE (E_υ^{NHE}) was estimated from the following equation: $E_\upsilon^{NHE} = E_\upsilon^f + \phi_{sp} + E_0^{NHE}$ where ϕ_{sp} is the work function of the spectrometer (4.37 eV) and E_0^{NHE} is the energy of the SHE with respect to vacuum level of the electron (−4.44 eV). From this E_υ^{NHE} value

and the optical band gap, the conduction band energy minimum (E_c^{NHE}) of the perovskites can be also determined. Referenced to the NHE, the VBM potentials were 1.95, 1.97 and 2.06 V for IEF-15, IEF-16 and IEF-17, respectively (Fig. 5a). Using the estimated band gap values, the position of conduction band minimum (CBM) can be assessed, obtaining the energy band diagrams of the perovskite materials (Fig. 5a). Thus, the better performance of IEF-16 could be explained by its more negative conduction band potential (-0.12 V) compared to IEF-15 (0.18 V) or IEF-17 (-0.07 V) along with a lower percentage of electron-hole recombination (the PL quenching of IEF-16 is more significant than that IEF-17, Figure 4b) and a higher photocurrent response (Fig. 5b). Finally, compared with other reported bismuth-based perovskites, the VBM of IEF-16 is more positive than that of $[(CH_3)_2NH_2]_3[BiI_6]$ (1.97 V vs 1.29 V), explaining why IEF-16 is a more efficient photocatalyst for OWS than $[(CH_3)_2NH_2]_3[BiI_6]$ [21].

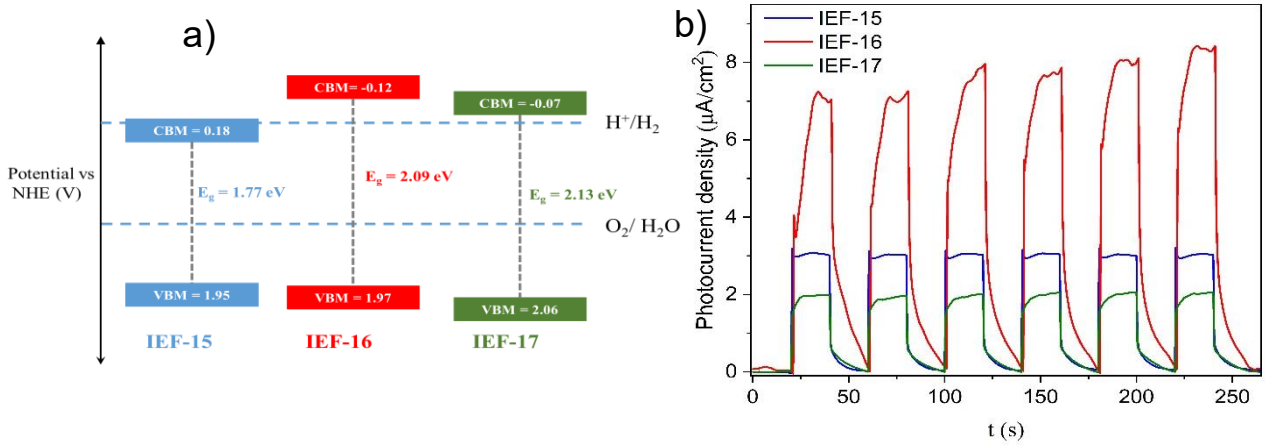

Figure 5. a) Energy level diagram for IEF-15, IEF 16 and IEF-17 samples and the standard reduction potential for O_2/H_2O and the standard oxidation potential for H^+/H_2 and b) Photocurrent responses of IEF-15, IEF 16 and IEF-17 samples during the on–off cycling and using an AM 1.5G light filter

In view of the superior performance of IEF-16, additional experiments were performed to optimize the experimental conditions (temperature, water volume, film preparation). Increasing the temperature at 80 and 150 ºC, the H_2 production rates of IEF-16 were 2.67 and 4.73 times higher than those obtained at 35 ºC (Fig. S13), which could be explained by an increase in the vapor pressure inside the reactor by the temperature. XRD analysis of IEF-16 after the reaction proved the good thermal stability of IEF-16 (Fig. S14). Concerning the influence of water volume on the H_2 activity (Fig. S15), a 6.8-fold increase of the activity was observed by decreasing the water content (5 *vs*. 0.1 mL), also maintaining its stability (Fig. S16). Note that the enhancement of H_2 production confirms the direct relationship between the increase in the water vapor pressure inside the reactor and the H_2 activity.

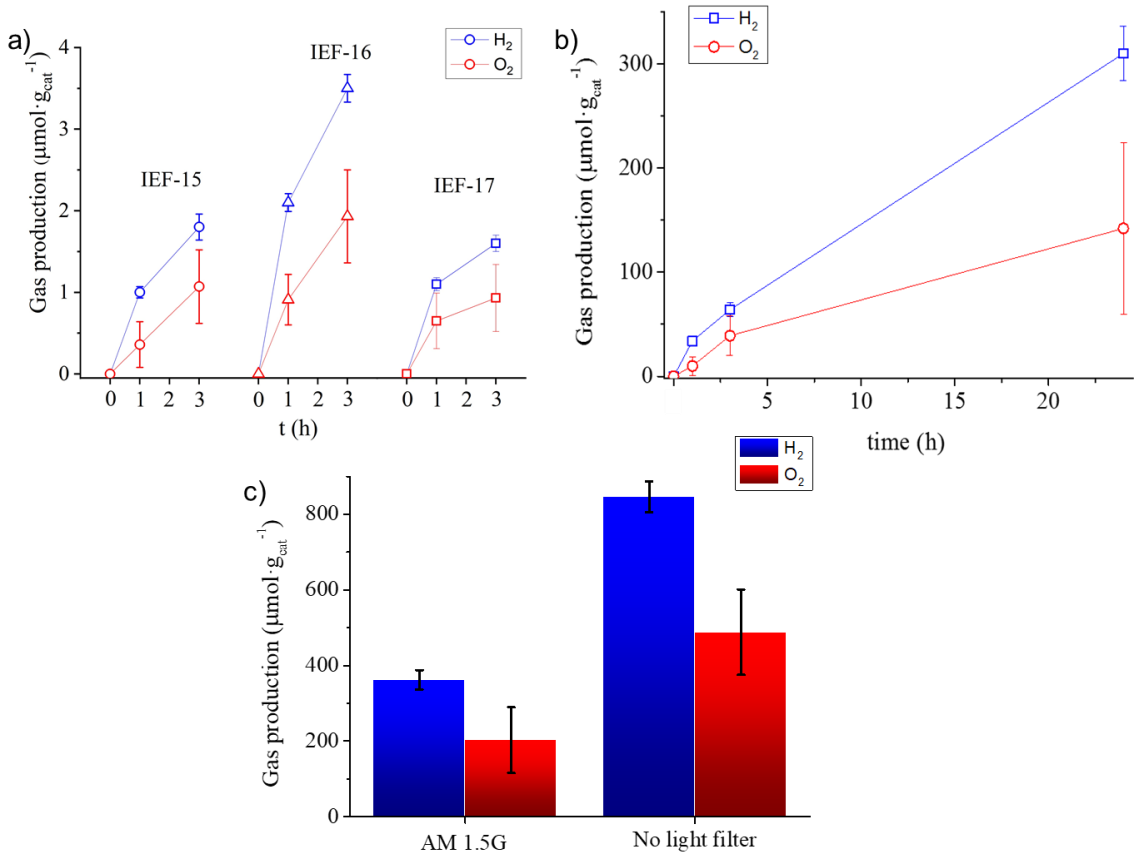

Fig. 6 a) Photocatalytic water splitting of powdered IEF-15 (○), IEF-16 (Δ) and IEF-17 (□) under simulated solar light irradiation. b) Photocatalytic hydrogen (blue) and oxygen (red) production from water using an IEF-16 thin film. c) Comparison of the photocatalytic OWS of IEF-16 film under simulated light (AM 1.5 G light filter) or UV-vis irradiation (without AM 1.5 G filter).

To further optimize the performance of IEF-16, we investigated its photocatalytic activity in the OWS by fabricating a thin film working under vapor conditions (Fig. 6b). Thin films are beneficial from the photocatalytic point of view by at least three features: i) favoring the water-photocatalyst contact surface, ii) increasing the number of photocatalytic active sites by better exposure of the material to the light, and iii) optimizing the amount of photocatalyst. Thus, IEF-16 was deposited on a glass substrate by a simple and efficient spin-coating method. As can be seen in Fig. 7a, the crystallization of the perovskite material over the substrate takes place with the formation of a homogeneous film with a thickness of 450 nm (see AFM measurements; Fig. S17). It is important to note that the IEF-16 film absorbs in the visible range with a maximum absorption band at 520 nm, promoting its use as an efficient visible-light photocatalyst (Fig. S18). Also, the moisture resistance of the IEF-16 thin film was monitored by XRD exposing the film to a high relative humidity (RH = 70%; Fig. 7b). The IEF-16 structure remains unaltered after 5 days, proving to be a moisture-stable perovskite compatible with the OWS reaction.

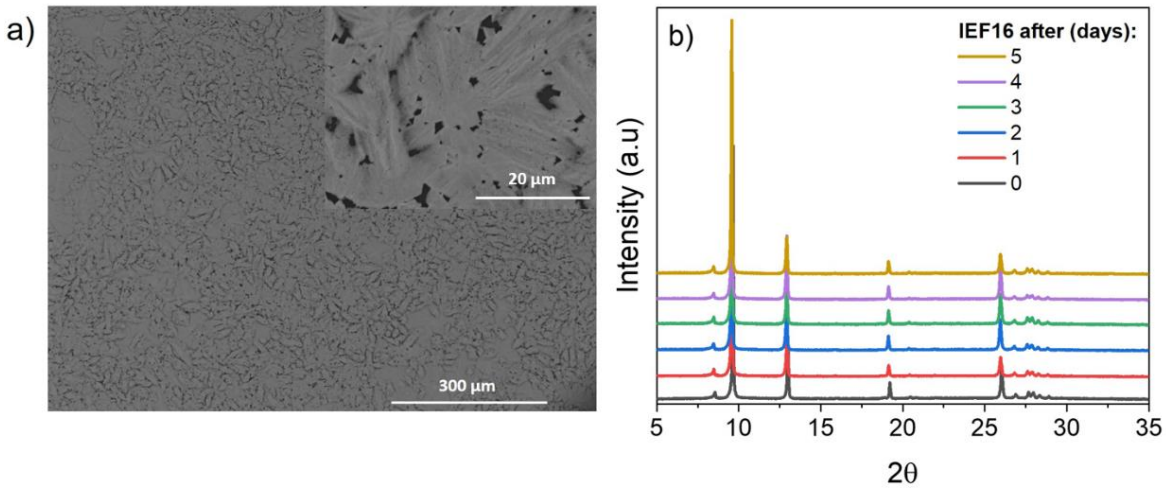

Fig. 7 a) SEM images of IEF-16 film and b) XRD patterns of the IEF-16 thin film under 70% RH over time.

Remarkably, IEF-16 film exhibited a significant photocatalytic hydrogen production *via* OWS, achieving 840 µmol $H_2 \cdot g^{-1}$ under UV-Vis irradiation and 360 µmol $H_2 \cdot g^{-1}$ under simulated solar light at 24 h (Fig. 6c). To verify the occurrence of an overall water-splitting mechanism, the oxygen evolution from H_2O was confirmed by using the labelled $H_2{}^{18}O$ and monitoring oxygen evolution during the experiment *via* mass spectrometry. In the resulting mass spectrum, a peak at m/z = 36 appears, corresponding to $^{18}O_2$ and confirming the $H_2{}^{18}O$ as a source of this photoproduct (Fig. S19). In addition, the OWS reaction was repeated on two more additional 24-h cycles, observing only a slight decrease in the H_2 activity, from 360 to 338 µmol$\cdot H_2 \cdot g^{-1}$ (Fig. S20). The H_2 activity of IEF-16 (34.5 µmol $g^{-1} \cdot h^{-1}$) in OWS is better than that reported for other perovskite-based photocatalysts as $[(CH_3)_2NH_2]_3[BiI_6]$ (30 µmol $g^{-1} \cdot h^{-1}$) by HI-splitting [19], $Rb_3Bi_2I_9$ (31.7 µmol g^{-1})·and $FA_3Bi_2I_9$ (20.09 µmol g^{-1}) in MeOH electrolyte [55], and $DMASnI_3$ (0.64 µmol g^{-1}) in deionized water [56]. Interestingly, only $DMASnI_3$ has reported photocatalytic activity in deionized water, forming SnI_4 due to the action of O_2 evolved in the process.

Further, the structure of the IEF-16 film is maintained after the 3 cycles (Fig. S21), despite the appearance of two small diffraction peaks at 72 h (2θ = 29.6 and 31.6º) corresponding to the partial hydrolysis and formation of a small fraction of BiOI, as previously reported by Hoye *et al*. who concluded that methylammonium bismuth iodide under air tends to be degraded into BiOI or Bi_2O_3, and not BiI_3 [50].

4. Conclusions

Three novel robust Bi(III)-hybrid perovskites have been synthesized based on 1D iodobismuthate chains (*i.e.* $[BiI]_5$ or $[BiI_4]$) and hydrophobic triazolium-TrzH or dimethylpyrazolium-DmpzH cations). Their full (structural, compositional, optical) characterization evidenced a high chemical stability together with appropriated valence and conduction bands position for both oxidation and reduction water reactions and reduced rate of charge recombination, proving to be active photocatalysts for H_2 production by the overall water splitting in absence of sacrificial agents. Outstandingly, upon thin film shaping of one of the solids, the TrzH$[BiI_4]$ or IEF-16, revealed an enhanced activity for OWS in comparison with other perovskite-based photocatalysts and an excellent stability under working conditions. Our findings provide valuable insights into the potential of bismuth-based hybrid perovskites as photocatalysts for environmental and energy applications.

Acknowledgments

A. J. C-G, Y. P. and P. H. acknowledge the National MICIU project Retos ‘‘MOFseidon’’ PID2019-104228RB-I00, Strategic Projects Oriented to Ecological Transition and Digital Transition “H2-MOF” TED2021-132092B-C21 and MADRID-PV2-CM/ EMT-4308 project from Comunidad de Madrid. S.N. thanks the support of grant PID2021-123856OBI00 funded by MCIN/AEI/ 10.13039/501100011033 and by ERDF A way of making Europe.

Electronic Supplementary Material: Supplementary material (additional figures PXRD, HRTEM, FT-IR, RAMAN, XPS, DR-UV-vis, TGA, UPS, H_2 activities, AFM analysis, mass spectrum of oxygen evolution, reusability test and crystallographic data) is available in the online version of this article at https

References

[1] European Comission. 2050 long-term strategy.

[2] Hosseini, S. E.; Wahid, M. A. Hydrogen production from renewable and sustainable energy resources: Promising green energy carrier for clean development. *Renew Sustain. Energy Rev.* **2016**, *57*, 850–866.

[3] Guerra, O. J.; Eichman, J.; Kurtz, J.; Hodge, B. M. Cost Competitiveness of Electrolytic Hydrogen. *Joule* **2019**, *3*, 2425–2443.

[4] Megia, P. J.; Vizcaino, A. J., Calles, J. A.; Carretero, A. Hydrogen Production Technologies: From Fossil Fuels toward Renewable Sources. A Mini Review. *Energy Fuels* **2021**, *35,* 16403–16415.

[5] Song, H.; Luo, S.; Huang, H.; Deng, B.; Ye, J. Solar-Driven Hydrogen Production: Recent Advances, Challenges, and Future Perspectives. *ACS Energy Lett.* **2022,** *7,* 1043–1065.

[6] Corredor, J.; Rivero, M. J.; Rangel, C. M.; Gloaguen, F.; Ortiz, I. Comprehensive review and future perspectives on the photocatalytic hydrogen production. *J. Chem. Technol. Biotechnol.* **2019**, *94*, 3049–3063.

[7] Cao, S.; Piao, L.; Chen, X. Emerging Photocatalysts for Hydrogen Evolution. *Trends Chem.* **2020**, *2*, 57–70.

[8] Zhang, H.; Ji, X.; Yao, H.; Fan, Q.; Yu, B.; Li, J. Review on efficiency improvement effort of perovskite solar cell. *Sol Energy* **2022**, *233*, 421–434.

[9] Best research-cell efficiencies. NREL 2023.

[10] Chin, X. Y.; Cortecchia, D.; Yin, J.; Bruno, A.; Soci, C. Lead iodide perovskite light-emitting field-effect transistor. *Nat Commun* **2015**, *6*, 1–9.

[11] Xiao, Z.; Kerner, R. A.; Zhao, L.; Tran, N. L.; Lee, K. M.; Koh, T.-W.; Scholes, G. D.; Rand, B. P. Efficient perovskite light-emitting diodes featuring nanometre-sized crystallites. *Nat. Photonics* **2017**, *11,* 108–115.

[12] Fu, X.; Jiao, S.; Dong, N.; Lian, G.; Zhao, T.; Lv, S.; Wang, K.; Cui, D. A. $CH_3NH_3PbI_3$ film for a room-temperature NO_2 gas sensor with quick response and high selectivity. *RSC Adv.* **2017**, *8*, 390–395.

[13] Zhao, Z.; Wu, J.; Zheng, Y.; Li, N.; Li. X.; Ye Z.; Lu, S.; Tao, X.; Chen, C. Environmental Stable hybrid perovskite $MAPb(I_{1-x}Br_x)_3$ for photocatalytic hydrogen evolution. *Appl. Catal. B Environ.* **2019**, *253*, 41–48.

[14] Ren, M.; Qian, X.; Chen, Y.; Wang, T.; Zhao, Y. Potential lead toxicity and leakage issues on lead halide perovskite photovoltaics. *J. Hazard Mater.* **2022**, *426*, 127848.

[15] Jin, Z.; Zhang, Z.; Xiu, J.; Song, H., Gatti, T.; He, Z. A critical review on bismuth and antimony halide based perovskites and their derivatives for

photovoltaic applications: recent advances and challenges. *J. Mater. Chem. A* **2020**, *8*, 16166–16188.

[16] Rajput, P. K.; Poonia, A. K.; Mukherjee, S.; Sheikh, T.; Shrivastava, M.; Adarsh, K. V.; Nag, A. Chiral Methylbenzylammonium Bismuth Iodide with Zero-Dimensional Perovskite Derivative Structure. *J. Phys. Chem. C* **2022**, *126*, 9889–9897.

[17] Li, M.-Q.; Hu, Y.-Q., Bi, L.-Y.; Zhang, H.-L.; Wang, Y.; Zheng. Y.-Z. Structure Tunable Organic–Inorganic Bismuth Halides for an Enhanced Two-Dimensional Lead-Free Light-Harvesting Material. *Chem. Mater.* **2017**, *29*, 5463–5467.

[18] Zhuang, R.; Wang, X.; Ma, W.; Wu, Y.; Chen, X.; Tang, L.; Zhu, H.; Liu, J.; Wu, L.; Zhou, W.; Liu, X.; Yang, Y.M. Highly sensitive X-ray detector made of layered perovskite-like $(NH_4)_3Bi_2I_9$ single crystal with anisotropic response. *Nat. Photonics* **2019**, *13*, 602–608.

[19] Zhao, H.; Li, Y.; Zhang, B.; Xu, T.; Wang, C. $PtI_x/[(CH_3)_2NH_2]_3[BiI_6]$ as a well-dispersed photocatalyst for hydrogen production in hydroiodic acid. *Nano Energy* **2018**; *50*, 665–674.

[20] Guo, Y.; Liu, G.; Li, Z.; Lou, Y.; Chen, J.; Zhao, Y., Stable Lead-Free $(CH_3NH_3)_3Bi_2I_9$ Perovskite for Photocatalytic Hydrogen Generation. *ACS Sustainable Chem. Eng.* **2019***, 7,* 15080−15085.

[21] Zhao, H.; Chordiya, K.; Leukkunen, P.; Popov, A.; Kahaly, M. U.; Kordas K.; Ojala S. Dimethylammonium iodide stabilized bismuth halide perovskite photocatalyst for hydrogen evolution. *Nano Res.* **2021**, *14*, 1116–1125.

[22] Li, Y., Zhuang, C., Qiu, S., Gao, J.; Zhou, Q.; Sun, Z.; Kang, Z.; Han, X. Cs-Cu-Cl perovskite quantum dots for photocatalytic H2 evolution with super-high stability. *Appl. Catal. B Environ.* **2023**, *337*, 122881.

[23] Liu, X.; Zhang, Q.; Zhao, S.; Wang, Z.; Liu, Y.; Zheng, Z.; Cheng, H.; Dai, Y.; Huang, B.; Wang, P.; Integrating Mixed Halide Perovskite Photocatalytic HI Splitting and Electrocatalysis into a Loop for Efficient and Robust Pure Water Splitting. *Adv. Mater.* **2023**, *35*, 2208915.

[24] Wu, Y.; Wu, Q.; Zhang, Q.; Lou, Z.; Liu, K.; Ma, Y.; Wang, Z.; Zheng, Z.; Cheng, H.; Liu, H.; Dai, Y.; Huang, B.: Wang, P. An organometal halide perovskite supported Pt single-atom photocatalyst for H_2 evolution. *Energy Environ. Sci.* **2022**, *15*, 1271–1281.

[25] García, T.; García-Aboal, R.; Albero, J.; Atienzar, P.; García, H. Vapor-phase photocatalytic overall water splitting using hybrid methylammonium copper and lead perovskites. *Nanomaterials* **2020,** *10*, 960-974.

[26] Bruker Apex2, Bruker AXS Inc. Madison Wis USA 2004.

[27] Sheldrick GM. SADABS, Software for Empirical Absorption Correction. Inst Inorg Chem Univ Gottingen Ger 1996.

[28] Altomare, A.; Burla, M.C.; Camalli, M.; Cascarano, G.L.; Giacovazzo, C. SIR97: a new tool for crystal structure determination and refinement. *J. Appl. Crystallogr* .**1999**, *32*, 115–119.

[29] Sheldrick GM. SHELX-2014, Program for Crystal Structure Refinement. Inst Inorg Chem Univ Gottingen Ger 2014.

[30] Farrugia, L.J. WinGX suite for small-molecule single-crystal crystallography. *J. Appl. Crystallogr.* **1999**, *32*, 837–838.

[31] Dolomanov, O. V., Bourhis, L. J., Gildea, R. J.; Howard, A. K.; Puschmann, H. OLEX2: a complete structure solution, refinement and analysis program. *J. Appl. Crystallogr.* **2009**, *42*, 339–341.

[32] Salcedo-Abraira, P.; Serrano-Nieto, R.; Biglione, C.; Cabrero-Antonino, M.; Vilela, S. M. F.; Babaryk, A. A.; Tilve-Martínez, D.; Rodriguez-Diéguez, A.; Navalón, S.; García, H.; Horcajada, P. Two Cu-Based Phosphonate Metal–Organic Frameworks as Efficient Water-Splitting Photocatalysts. *Chem. Mater.* **2023**, *35*, 4211–4219.

[33] Oswald, I. W. H.; Ahn, H.; Neilson, J.R. Influence of organic cation planarity on structural templating in hybrid metal-halides. Dalton Trans. **2019**, *48,* 16340–16349.

[34] Shestimerova, T. A.; Mironov, A. V.; Bykov, M. A.; Starichenkova, E. D.; Kuznetsov, A. N.; Grigorieva, A. V.; Shevelkov, A. V. Reversal Topotactic Removal of Acetone from $(HMTH)_2BiI_5 \cdot (CH_3)_2C{=}O$ Accompanied by Rearrangement of Weak Bonds, from 1D to 3D Patterns. Cryst. Growth Des. **2020**, *20*, 87–94.

[35] Li, T.; Hu, Y.; Morrison, C. A.; Wu, W.; Hana, H.; Robertson, N. Lead-free pseudo-three-dimensional organic-inorganic iodobismuthates for photovoltaic applications. Sustain. Energy Fuels **2017**, *1*, 308–316.

[36] Skorokhod, A.; Mercier, N.; Allain, M.; Manceau, M.; Katan, C.; Kepenekian, M. From Zero- to One-Dimensional, Opportunities and Caveats of Hybrid Iodobismuthates for Optoelectronic Applications. *Inorg. Chem.* **2021**, 60, 17123–17131.

[37] Ma, Z.; Peng, S.; Wu, Y.; Fang, X.; Chen, X.; Jia, X.; Zhang, K.; Yuan, N.; Ding, J.; Dai, Ning. Air-stable layered bismuth-based perovskite-like materials: Structures and semiconductor properties. *Phys. B Condens. Matter.* **2017**, *526*, 136–142.

[38] Jain, S. M., Phuyal, D., Davies, M. L., Li, M.; Philippe, B.; Castro, C.; Qui, Z.. An effective approach of vapour assisted morphological tailoring for reducing metal defect sites in lead-free, $(CH_3NH_3)_3Bi_2I_9$ bismuth-based perovskite solar cells for improved performance and long-term stability. *Nano Energy* **2018**, 49, 614–624.

[39] Babaryk, A. A.; Pérez, Y.; Martínez, M.; Mosquera, M. E. G.; Zehender, M. H.; Svatek, S. A.; Antolín, E.; Horcajada, P. Reversible dehydration-

hydration process in stable bismuth-based hybrid perovskites. *J. Mater. Chem. C* **2021**, *9*, 11358–11367.

[40] Albero, J.; Asiri, A. M.; García, H. Influence of the composition of hybrid perovskites on their performance in solar cells. *J Mater Chem A* **2016**, *4*, 4353–4364.

[41] Castelli, I. E.; García-Lastra J. M.; Thygesen, K. S.; Jacobsen, K. W. Bandgap calculations and trends of organometal halide perovskites. *APL Mater.* **2014**, *2,* 081514.

[42] Kim, S.-Y.; Yun, Y.; Shin, S.; Lee, J.H.; Heo, Y.-W.; Lee, S. Wide range tuning of band gap energy of $A_3B_2X_9$ perovskite-like halides. *Scr Mater* **2019**, *166,* 107–111.

[43] Jena, A. K.; Kulkarni, A.; Miyasaka, T. Halide Perovskite Photovoltaics: Background, Status, and Future Prospects. *Chem. Rev.* **2019**, *119*, 3036–3103.

[44] Zhang, H. Y.; Wei, Z.; Li, P. F.; Tang, Y. Y.; Liao, W.-Q.: Ye, H.-Y.: Cai, H. Xiong, R.-G. The Narrowest Band Gap Ever Observed in Molecular Ferroelectrics: Hexane-1,6-diammonium Pentaiodobismuth(III). *Angew. Chem. - Int. Ed.* **2018**, 57, 526–530.

[45] Tao, K.; Li, Y.; Ji, C.; Wu, Z.; Han, S.; Sun, Z.; Luo, J. A. Lead-Free Hybrid Iodide with Quantitative Response to X-ray Radiation. *Chem. Mater.* **2019**, *31*, 5927–5932.

[46] Fan, Z.; Xiao, H.; Wang, Y.; Zhao, Z.; Lin, Z.; Cheng, H.-C.; Lee, S.-J.; Wang, G.; Feng, Z.; Goddard III, W. A.; Huang, Y.; Duan, X. Layer-by-Layer Degradation of Methylammonium Lead Tri-iodide Perovskite Microplates. *Joule* **2017**, *1*, 548–562.

[47] Kotov, V. Y.; Ilyukhin, A. B.; Korlyukov, A. A.; Smol`yakov, A. F.; Kozyukhin, S. A. Black hybrid iodobismuthate containing linear anionic chains. *New J Chem* **2018**, *42*, 6354–6363.

[48] García-Fernández, A.; Marcos-Cives, I.; Platas-Iglesias, C.; Castro-García, S.; Vázquez-García, D.; Fernández, A.; Sánchez-Andújar, M. Diimidazolium Halobismuthates $[Dim]_2[Bi_2X_{10}]$ (X = Cl^-, Br^-, or I^-): A New Class of Thermochromic and Photoluminescent Materials. *Inorg. Chem.* **2018**, *57*, 7655–7664.

[49] Dennington, A.J.; Weller, M.T. Synthesis and structure of pseudo-three dimensional hybrid iodobismuthate semiconductors. *Dalton Trans.* **2016**, *45*, 17974–17979.

[50] Hoye, R. L. Z.; Brandt, R. E.; Osherov, A.; Stevanovic, V.; Stranks, S. D.; Wilson, M. W. B.; Kim, H.; Akey, A. J.; Perkins, J. D.; Kurchin, R. C.; Poindexter, J. R. Wang, E. N.; Buonassisi, T. Methylammonium Bismuth Iodide as a Lead-Free, Stable Hybrid Organic–Inorganic Solar Absorber. *Chem. – Eur. J.* **2016**, *22*, 2605–2610.

[51] Fu, W.; Ricciardulli, A. G.; Akkerman, Q. A.; John, R. A.; Tavakoli, M.M.; Essig, S.; Saliba, M.; Stability of perovskite materials and devices. *Mater. Today* **2022**, *58*, 275-296.

[52] Li, X.-L.; Gao, L.-L.; Ding, B.; Chu, Q.-Q.; Li, Z.; Yang, G.-H. ($C_6H_5NH_3$)BiI_4: a lead-free perovskite with >330 days humidity stability for optoelectronic applications. *J. Mater. Chem. A* **2019**, *7*, 15722–15730.

[53] Han, L.; Wang, P.; Wu, Q.; Wang, Z.; Liu, Y.; Zheng, Z.; Cheng, H., Dai, Y.; Huang, B. Design the π-stacking type of perovskite-like iodobismuthates to enhance their optoelectronic properties. *J. Mol. Struct.* **2022**, *1247*, 131332.

[54] Ji, F.; Klarbring, J.; Wang, F.; Ning, W.; Wang, L.;- Yin, C.; Figueroa, J.S.M Christensen, C.K.; Etter, M.; Ederth, T.; Sun, L.; Simal, S.I.; Abrikosov, I.A.; Gao, F.;. Lead-Free Halide Double Perovskite $Cs_2AgBiBr_6$ with Decreased Band Gap. *Angew. Chem. Int. Ed.* **2020**; *59*: 15191–15194.

[55] Miodyńska, M.; Klimczuk, T.; Lisowski, W.; Zaleska-Medynska, A. Bi-based halide perovskites: Stability and opportunities in the photocatalytic approach for hydrogen evolution. *Catal. Commun.* **2023**, *177*, 106656.

[56] Ju, D.; Zheng, X.; Liu, J.; Chen, Y.; Zhang, J.; Cao, B.; Xiao, H.; Mohammed, O. F.; Bakr, O.M.; Tao, X. Reversible Band Gap Narrowing of Sn-Based Hybrid Perovskite Single Crystal with Excellent Phase Stability. *Angew. Chem. Int. Ed.* **2018**, *57*, 14868–14872.